Int. J. Electrochem. Sci., 14 **(2019)** 5846 – 5855, doi: 10.20964/2019.06.78

International Journal of
ELECTROCHEMICAL
SCIENCE
www.electrochemsci.org

Effects of Mg Partial Substitution for Pr on the Electrochemical Performances of Pr-Mg-Ni-based Alloys

Jianzhi Dou[1,†] , *Jingxuan Wei*[2,†], *Peng Wang*[3], *Zhijie Gao*[4,*]

[1] School of Applied Chemistry, Food and Pharmacy, Weifang Engineering Vocational College, Qingzhou 262500, PR China
[2] Binzhou Polytechnic, Binzhou, 256600, PR China
[3] College of Airport, Binzhou University, Binzhou 256600, PR China
[4] School of Automotive Engineering, Shandong Jiaotong University, Jinan 250023, PR China
[†] These authors contributed equally to this work
[*]E-mail: gaozhijie1983@126.com

Received: 16 March 2019 / *Accepted:* 23 April 2019 / *Published:* 10 May 2019

The influences of Mg substitution for Pr on the phase structures, hydrogen desorption characteristics and electrochemical properties of $Pr_{1-x}Mg_xNi_{3.1}Co_{0.3}Al_{0.1}$ (x = 0.0, 0.1, 0.15, 0.17, 0.2, 0.25, 0.3) alloys have been investigated. Partial replacement of Mg for Pr promotes the formation of super-stacking phases, refines crystal grains and decreases cell volumes. When $x \leqslant 0.2$, the alloys consist of a main Ce_2Ni_7-type $(Pr,Mg)_2Ni_7$ phase and a few $CaCu_5$-type $PrNi_5$ phase. As Mg content further increases, the alloys mainly contain Ce_2Ni_7-type $(Pr,Mg)_2Ni_7$, $PuNi_3$-type Pr_2MgNi_9 and $CaCu_5$-type $PrNi_5$ phases. The plateau pressure of hydrogen desorption is initially increased and then decreased by the substitution and the reversibility is enhanced. Electrochemical analysis shows that the cycling stability for the alloy with x = 0.15~0.17 reaches 87.8% after 100 charge/discharge cycles. Meanwhile the maximum discharge capacity is improved. Further study shows that Mg increases the ratio of super-stacking structures so that the discharge capacity is enhanced. Mg optimize P_{eq} by adjusting the cell volumes of the phases so as to ameliorate the electrochemical performances. Alloys with x = 0.15~0.17 shows the optimal electrochemical performances.

Keywords: Pr-Mg-Ni-based hydrogen storage alloy, Mg substitution, Microstructure, Electrochemical properties

1. INTRODUCTION

La–Mg–Ni-based alloys are recognized to be one of the most hopeful negative electrode materials for nickel/metal hydride batteries due to their high discharge capacity (~410 mAh g^{-1}) [1], superior high rate dischargeability [2, 3], environmental friendliness [4] and other advantages [5]. However, their discharge capacity, cycling stability, and self-discharge properties, especially cycling

stability need to be further improved, which can be satisfied the urgent demand for a power source with favorable overall electrochemical performance.

It is well known that ternary La-Mg-Ni compounds originated from corresponding binary La-Ni compounds have been investigated [6, 7]. The inferior cycling stability of La-Mg-Ni-based alloy electrodes is mainly originated from oxidation/corrosion and pulverization of the active componets during cycling. Therefore, rare earth element Pr, Nd, Sm or Gd with lower chemical activity is used to partly replace La element in the La-Mg-Ni-based alloys. Recently, the substituting method in which Pr or Nd as the only rare earth element is used has paid close attention. This is both a basic interest and a potential application. [8, 9, 10]. However, the wide application of alloys due to their inferior cycling stability has been restricted [11, 12].

It has been reported that ternary Pr-Mg-Ni alloys exhibited superior gas-solid hydrogenation properties. Iwase et al. found that the maximum hydrogen capacity of Pr_3MgNi_{14} alloy was 1.12 H/M (1.61 mass %) at 298 K and its retention rate after 1000 cycles reached to 87.5%, which compared favorably with that of $LaNi_5$ [13]. Although some ternary Pr-Mg-Ni-based alloys have showed superior gas-solid hydrogenation properties [14, 15, 16], little is known about their electrochemical properties.

Magnesium is a key element in the RE-Mg-Ni-based alloys plus cheap and light weight [17, 18]. It exclusively enters [La2Ni4] subunits to promote the formation of the phases with super-stacking structures such as $(La,Mg)Ni_3$, $(La,Mg)_2Ni_7$ and $(La,Mg)_5Ni_{19}$ phases [19, 20]. By adjusting the stability of hydride, the Mg content has a significant effect on the hydrogenation/dehydrogenation behavior of La-Mg-Ni based alloys [21]. In addition, Mg helps to reduce the stacking faults of trapping hydrogen atoms, thereby hindering the hydrogen absorption/desorption process. [22, 23]. In spite of that, as the content of Mg further increases, the cycling stability of the alloys will be jeopardized due to its low corrosion resistance and its tendency to form high-Mg phases. Therefore, a proper element favoring the cycling stability of the La-Mg-Ni-based alloys is needed to cooperate with Mg. However, the influence of the solid solubility of Mg atoms in the A_2B_7 type phase Pr-Mg-Ni alloy and the substitution of Pr for various Mg amounts of structural changes and hydrogen storage characteristics are still unclear.

Based on the discussion above, in this study, Mg are used to partially substitute for Pr in alloys The effects of the Mg-substitution on the phase evolution, hydrogen storage characteristics and electrochemical performances of the alloys are investigated. The function of Pr and Mg has been illustrated. It is expected that a proper amount of Mg substitution for Pr can effectively ameliorate the overall electrochemical performances, especially the cycling stability of the Pr–Mg–Ni–based alloys.

2. EXPERIMENTAL DETAILS

2.1 Sample Preparation

The alloys designed as $Pr_{1-x}Mg_xNi_{3.1}Co_{0.3}Al_{0.1}$ (x = 0.0, 0.1, 0.15, 0.17, 0.2, 0.25, 0.3) were prepared by the induction melting method at 0.4 MPa of Ar atmosphere. The ingots were annealed for 8 hours at 1173 K under Ar pressure (0.1 MPa). A compensation of 5 wt.% of both Pr and Mg was applied due to the burning loss. The purity of all elements was above 99.9 wt.%.

2.2 Structural and Electrochemical Characterization

The annealed alloy was mechanically pulverized into powder (<38 μm) for X-ray diffraction (XRD) measurement, and 54 to 61 μm powder was used for electrode testing. XRD measurements were performed on a Rigaku D / max-2400 diffractometer with Cu radiation and 40 kV x 150 mA power. The pattern was recorded in the range of 15° to 90° in which the step size of 2θ was 0.02°. Then the collected data were analyzed by the Rietveld method [24] using Fullprof 2000 software [25] to get the lattice parameters, site of Mg atoms and phase abundance. The backscattered electron images were obtained by Scanning electron microscope (SEM, JSM-5000LV) with energy dispersive spectroscopy (EDS) and Electron probe microanalyzer (EPMA-1600) with wave dispersive spectroscopy (WDS), which was used to characterize the phase structure and the composition of alloys.

The annealed alloy powders of ~0.1g were selected from 54 to 61 microns and the electrodes were prepared. The alloy electrode was synthesized by cold pressing the mixture of the alloy powder and nickel carbonyl powder at a weight ratio of 1:3 under 20 MPa pressure to form anodes with a diameter of 10 mm. The electrochemical measurements were carried out at 298K in a standard open three-electrode cell. The cell consists of an alloy electrode, a sintered $Ni(OH)_2$/NiOH cathode and a Hg/HgO reference electrode immersed in 6M KOH electrolyte. Discharge each electrode to the cut-off potential -0.6 V vs. Hg/HgO reference electrode. During the activation process, the electrode was charged/discharged at a current density of 60 mA g^{-1}. When the cycle stability at 298 K was checked, the electrode was charged/discharged at a current density of 300 mA g^{-1}.

2.3 Hydrogen Absorption and Desorption

Since the hydrogen absorption/desorption plateau of RE-Mg-Ni alloy system is low [26], the self-discharge problem can be neglected if the electrode test time is not long. Therefore, the P-C isotherm can be determined by electrochemical method according to Nernst equation [28].

$$E_{eq} \text{ vs. Hg/HgO} = -0.93-0.0296 \log(Peq) \text{ at } 298 \text{ K} \quad (1)$$

The equilibrium potential (E_{eq}) was determined by alternately performing the following operation: (a) a pulse capacity charge/discharge of 10 mAh g^{-1} with 60 mA g^{-1} current density; (b) a rest period (about 20 min) for the potential to become constant.

3. RESULTS AND DISCUSSION

3.1 Alloy crystal structure

Fig. 1 shows the XRD patterns for $Pr_{1-x}Mg_xNi_{3.1}Co_{0.3}Al_{0.1}$ (x = 0.0, 0.1, 0.15, 0.17, 0.2, 0.25, 0.3) alloys. According to the Rietveld refinement analyses, the abundance of phase was tabulated in Table 1. The main phases for x = 0 consist mainly of Pr_2Ni_7 (Ce_2Ni_7-type, SG: $P6_3/mmc$) phase, and $PrNi_5$ ($CaCu_5$-type, SG: P6/mmm) phase. As Mg content increases, the main phase of all of the alloys can be indentified as Ce_2Ni_7-type phase just as shown in Fig. 1. Moreover, the abundance of $PrNi_5$ phase decreases from 20.51 wt.% (x = 0.0) to 2.2 wt.% (x = 0.15~0.17). Since the abundance of $PrNi_5$ phase in the alloys of x = 0.15, 0.17 is very small, it is difficult to be observed in the back scattering electron

images just as shown in Fig. 2. Furthermore, when x > 0.2, the $PuNi_3$-type Pr_2MgNi_9 phase appears, the abundance of which are 8.25 wt.% (x = 0.25) and 39.21 wt.% (x = 0.3). Fig. 2 presents the back scattering electron images of the alloy with x = 0.0, 0.15, 0.3 as typical examples. There are four regions in the image which are dark grey, grey and light grey, white. Combining EDS analysis with Rietveld analysis, white region (C area) can be identified as $PrNi_5$ phase, dark grey region (D area) can be identified as $PuNi_3$-type Pr_2MgNi_9 phase and the rest regions (A and B) can be identified as Ce_2Ni_7-type $(Pr,Mg)_2Ni_7$ phase. Based on the above analysis, it is also clear that the alloy of x = 0.15 exhibits good single phase. Presence of Pr_2MgNi_9 phase indicate that the Ce_2Ni_7-type crystal structure may disintegrate as Mg content increases, which are attributed to the following reaction: $2(Pr,Mg)_2Ni_7 \rightarrow 3(Pr,Mg)Ni_3 + LaNi_5$. As a result, $(Pr,Mg)Ni_3$ phase contains more Mg content with increasing Mg content. These observations are consistent with the former reported by La-Mg-Ni-based alloy [6, 8, 9].

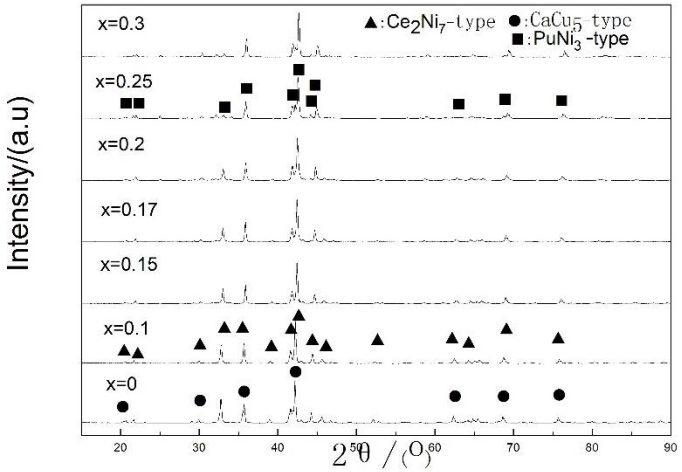

Figure 1. XRD patterns for $Pr_{1-x}Mg_xNi_{3.1}Co_{0.3}Al_{0.1}$ (x = 0.0, 0.1, 0.15, 0.17, 0.2, 0.25, 0.3) alloys

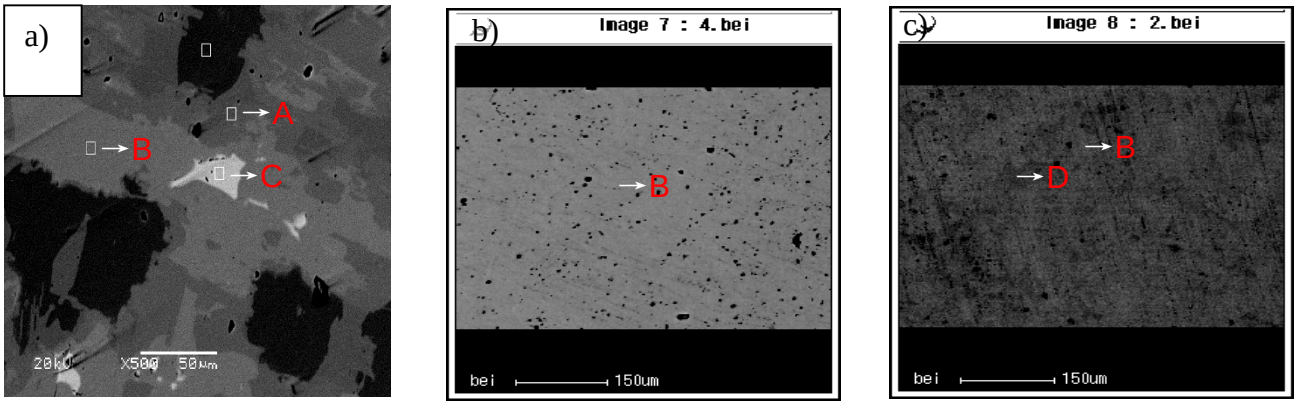

Figure 2. Back scattered electron images for $Pr_{1-x}Mg_xNi_{3.1}Co_{0.3}Al_{0.1}$ alloys: a) x = 0.0, b) x = 0.15, c) x = 0.3: (A and B: $(Pr,Mg)_2Ni_7$ phase, C: $PrNi_5$ phase, D: Pr_2MgNi_9 phase)

Table 1 also tabulates the lattice parameters of alloys as a function of Mg content x, it can be seen that the lattice parameters and cell volumes of the $(Pr,Mg)_2Ni_7$ phase and $PrNi_5$ phase decrease

monotonously as x increase from 0 to 0.3. This is due to the fact that the atomic radii of the substituting elements Mg (136 pm) are smaller than that of Pr (182.8 pm).

Table 1. Characteristics of phases for $Pr_{1-x}Mg_xNi_{3.1}Co_{0.3}Al_{0.1}$ alloys.

Sample	Phase	a (Å)	c (Å)	V(Å^3)	c/a	Phase abundance (wt.%)
x = 0.0	$(Pr,Mg)_2Ni_7$	5.058	24.710	547.470	4.885	79.49
	$PrNi_5$	5.046	3.992	89.77	0.791	20.51
x = 0.15	$(Pr,Mg)_2Ni_7$	5.050	24.389	538.699	4.830	97.8
	$PrNi_5$	5.045	3.980	87.74	0.789	2.2
x = 0.3	$(Pr,Mg)_2Ni_7$	4.909	23.809	496.865	4.850	58.44
	Pr_2MgNi_9	5.038	24.250	532.567	4.813	39.21
	$PrNi_5$	5.046	3.768	83.110	0.747	2.35

Table 2. Crystallographic parameters of $Pr_{0.85}Mg_{0.15}Ni_{3.1}Co_{0.3}Al_{0.1}$ alloy with space groupP63/mmc

Atom	Symmetry	x	y	z	B_{iso}	Occupancy
Pr 1	4f	1/3	2/3	0.02698(8)	1.03(6)	0.69(1)
Pr 2	4f	1/3	2/3	0.17108(6)	0.98(4)	1.00(1)
Mg 1	4f	1/3	2/3	0.02698(8)	1.03(-)	0.31(-)
Ni 1	2a	0	0	0	0.90(1)	1.00(-)
Ni 2	4e	0	0	0.16780(1)	0.98(7)	1.00(-)
Ni 3	4f	1/3	2/3	0.83290(1)	0.61(6)	1.00(-)
Ni 4	6h	0.8326(8)	0.665(2)	1/4	0.50(6)	1.00(-)
Ni 5	12k	0.8330(5)	0.666(1)	0.08486(6)	0.84(4)	1.00(-)

According to Rietveld analysis, the crystallographic parameters of Ce_2Ni_7 cell for the alloy x = 0.15 are listed in Table 2. It is noteworthy that Mg atoms are located only at 4f position in Laves unit of Ce_2Ni_7 cell, which is similar to the distribution of Mg atoms in $PuNi_3$ cell. The actual composition ($Pr_{1.69}Mg_{0.31}Ni_7$) can be obtained according to the occupancy of Mg atoms in the cell, which is very consistent with the nominal composition. As can be seen from Table 2, another detail of the slight change in X and Y in atomic coordinates is shown in comparison with the crystal structure data of Pr_2Ni_7 alloy.

3.2 Thermodynamic (P-C isotherm) measurements

Fig. 3 shows the electrochemical P-C desorption isotherms of $Pr_{1-x}Mg_xNi_{3.1}Co_{0.3}Al_{0.1}$ (x = 0.0, 0.1, 0.15, 0.3) measured at 298K, and Table 3 summarizes the desorption characteristics of different alloys. The P-C isotherms show clear plateau regions due to the co-existence of α and β phases.

Table 3. Hydrogen absorption/desorption properties of $Pr_{1-x}Mg_xNi_{3.1}Co_{0.3}Al_{0.1}$ alloys

Alloy	Reversible hydrogen capacity (wt%)	C_{rev} (mAh/g)	P_d (MPa)
x = 0.0	0.63	152.8	0.003
x = 0.1	1.35	336.3	0.080
x = 0.15	1.44	348.6	0.140
x = 0.3	0.86	200.9	0.710

Reversible hydrogen storage capacity is the difference between maximum capacity and capacity at the end of hydrogen desorption. It can be found that the reversible hydrogen storage capacity firstly increase and then decrease as x increases from 0 to 0.3. The substitution improves the reversible hydrogen storage capacity of alloys. The factors affecting hydrogen storage capacity are as follows: Firstly, the total abundances of Ce_2Ni_7 and $PuNi_3$-type Pr_2MgNi_9 phase with superstacking structure [29] increase, and the $PrNi_5$ phase abundances decrease as x increases from 0 to 0.3. It is well known that the hydrogen storage capacities of $(Pr,Mg)_2Ni_7$ phase and Pr_2MgNi_9 phase are larger than that of the $PrNi_5$ phase. Large amount of hydrogen can be absorbed not only inside the $[A_2B_4]$ units but also between the $[AB_5]$ and $[A_2B_4]$ units in the super-stacking structures. The advantage brought by more super-stacking structures is note worthy. Furthermore, the reversible hydrogen storage capacity is related to the cell volumes of the phases. Because of the small space of hydrogen atoms, the reduction of cell volume reduces the amount of hydrogen absorbed. The synthesis effect of the above factors leads to the trend of reversible hydrogen storage capacity of the alloy. As the Mg content increases, the hydrogen desorption plateau becomes distinct. It can be seen that the plateau pressure of hydrogen desorption rises gradually from 0.003 to 0.710 MPa. This indicates that the increase of the Mg content modulates the stability of hydride phase due to the decrease of cell volume [6].

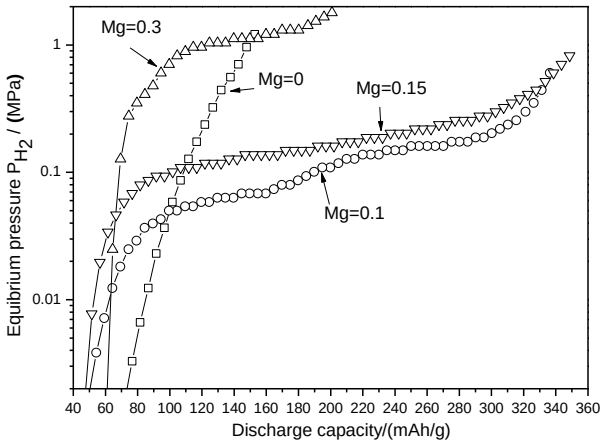

Figure 3. P-C isotherms of $Pr_{1-x}Mg_xNi_{3.1}Co_{0.3}Al_{0.1}$ (x = 0.0, 0.1, 0.15, 0.3) alloys at 298 K

3.3 Charge/discharge characteristics

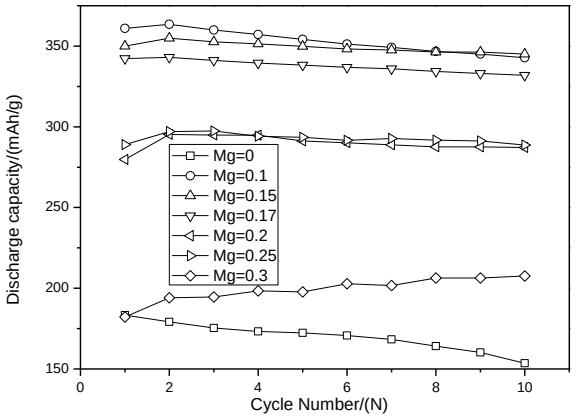

Figure 4. Activation curves of $Pr_{1-x}Mg_xNi_{3.1}Co_{0.3}Al_{0.1}$ (x = 0.0, 0.1, 0.15, 0.17, 0.2, 0.25, 0.3) annealed alloy electrodes with 60mA g^{-1} charge-discharge current density at 298 K

Fig. 4 shows the discharge capacities of the alloy electrodes before their discharge voltage decrease to 0.6 V. The results are listed in Table 4. It can be found that the alloy electrodes can be fully activated within three cycles except x = 0.3. The better activation property is due to the multi-phase structures of the alloys. The interface of the phases and the cracks formed in the alloys are helpful to the diffusion of the hydrogen atoms in the initial few cycles. The maximum discharge capacity of the alloy electrodes is increased from 180 mAh g^{-1} (x = 0.0) to 350 mAh g^{-1} (x = 0.1~0.17). The amelioration is ascribed to the increasing amount of super-stacking phases. The total amount of $(Pr,Mg)_2Ni_7$ phase increases from 79.49 wt.% (x = 0) to 97.8 wt.% (x = 0.15). But as x further increases, the maximum discharge capacity gradually decreases to 203.6 mAh g^{-1} (x = 0.3). It should be noted that the improving effect in C_{max} is not very significant and the C_{max} becomes smaller when x > 0.2. This is largely due to the contraction of the cell volumes, which decreases the room for hydrogen atoms.

Table 4. Summary of electrochemical performance for $Pr_{1-x}Mg_xNi_{3.1}Co_{0.3}Al_{0.1}$ annealed alloy electrodes at 298 K

Sample	N	C_{max}(mAh g^{-1})		S_{100}(%)
		60 mA g^{-1}	300 mA g^{-1}	
x = 0.0	1	180	120.4	88.7
x = 0.1	2	356	327.7	82.7
x = 0.15	2	348	333.2	87.8
x = 0.17	2	343	329.3	87.1
x = 0.2	2	289.5	284.5	84.8
x = 0.25	3	291.6	287.2	81.7
x = 0.3	10	203.6	224.1	86.6

3.4 Cycle stability

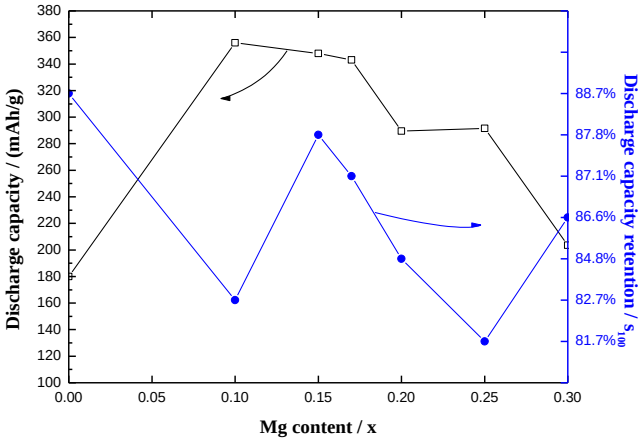

Figure 5. Discharge capacity and cycle life of $Pr_{1-x}Mg_xNi_{3.1}Co_{0.3}Al_{0.1}$ annealed alloy electrodes as a function of Mg content (x)

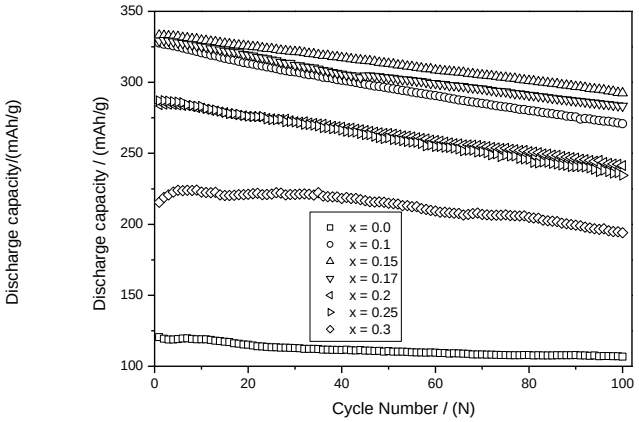

Figure 6. Cycle stability curves of $Pr_{1-x}Mg_xNi_{3.1}Co_{0.3}Al_{0.1}$ annealed alloy electrodes with $300mAg^{-1}$ charge-discharge current density at 298 K

Figs. 5 and 6 show the discharge capacity retention curves of $Pr_{1-x}Mg_xNi_{3.1}Co_{0.3}Al_{0.1}$ (x = 0.0, 0.1, 0.3, 0.4, 0.5, 1.0) alloy electrodes. In order to illustrate cycle stability, capacity retention rate at the 100th cycle (S_{100}) is calculated as the ratio of C_{100}/C_{max}, and is listed in Table 4. It can be found that the cycle stability of all alloy electrodes initially increases and then decreases as x increases from 0.1 to 0.25. The S_{100} of the alloy electrodes increases from 82.7% (x = 0.1) to 87.8% (x = 0.15). From the results it is indicated that the Mg partial substitution for Pr significantly improves the cycling stability of the alloy electrodes. The improvement is due to the refinement of the grain size and oxidation-resistance. It comes to light that pulverization is a fundamental reason for the capacity decay of the electrode alloys. Pulverization further causes severe oxidation. The anti-pulverization capability of the alloys basically depends on their grain size [30]. Furthermore, the order of anti-oxidation of alloys phase is $(Pr,Mg)_2Ni_7$ phase > Pr_2MgNi_9 phase [29, 31]. Thirdly, the order of electronegativity values of rare earth elements is Pr (1.13) > La (1.10) and it is known that partial substituting La with Pr can reduce the

oxidation in KOH. Pr should make contribution to the oxidation-resistance. In addition, during charge/discharge process, Mg addition can inhibit the amorphous tendency of the alloys [6].

However, as x exceeds 0.20, the cyclic stability is worsened. The first reason are caused by both the increasing content of Mg element which has poor corrosion resistance. Secondly, the ratio of $(Pr,Mg)_2Ni_7$ phase abundance to Pr_2MgNi_9 phase abundance decreases as x increases from 0.2 to 0.3. At the same time, the $PrNi_5$ phase of the alloys is gradually disappear. The phase abundance of $(Pr,Mg)_2Ni_7$ phase originated from substituting Pr with Mg gradually decreases for deteriorating the cycle stability of the alloy as Mg content rising.

Based on the above analysis, it can be concluded that a proper amount of Mg addition (x = 0.1~0.2) can improve the cycle stability of the alloy electrode owing to the better anti-pulverization capability and the lower amorphous tendency. However, the further increase of Mg content accelerates the difficulty to desorption H_2 and induces the deterioration of the cycle stability for the alloy electrodes.

4. CONCLUSIONS

The structure and electrochemical properties of Pr-Mg-Ni based alloys were systematically studied. Some conclusions can be drawn:

1) The main phase of x = 0.1-0.2 alloys is $(Pr,Mg)_2Ni_7$ phase with Ce_2Ni_7-type structure. As Mg content increases from x = 0.25 to x = 0.3, some $PuNi_3$-type Pr_2MgNi_9 phases appear. Mg atoms are occupied only at 4f position in a Ce_2Ni_7 cell.

2) P-C isotherms show that the hydrogen desorption capacity first increases from 0.63 wt.% to 1.44 wt.% and then decreases to 0.86 wt.% as x increases from 0 to 0.3. Meanwhile, hydrogen desorption plateau became first flatter and wider and then higher and narrower as x increase.

3) The favorable Mg content ranged from 0.15 to 0.17 results in the increase of maximum discharge capacity and the improvement of cycling stability for the alloy electrodes. It is ascribed to the increase of $(Pr,Mg)_2Ni_7$ phase and the addition of Mg suppresses the amorphization of the $PrNi_{3.5}$ alloy. The overall electrochemical properties of Pr-Mg-Ni-based alloys are improved by optimizing the composition, constituent phase structures and thermodynamic parameters of the superlattice alloys. The findings in this paper are expected to develope the novel Pr-Mg-Ni-based hydrogen storage alloys.

ACKNOWLEDGEMENTS
This work was supported by the Nature Science Foundation of Shandong Province (No. ZR2014EMP012, ZR2017QEE014), Doctor Foundation of Binzhou University (No. 2013Y10) and the Science and Technology Development Plan of Bingzhou (No. 2014ZC0216). The authors express sincere thanks to the NSFC (Natural Science Foundation of China, 51404220) for financial support.

References

1. T. Kohno, H. Yoshida, F. Kawashima, T. Inaba, I. Sakai, M. Yamamoto and M. Kanda, *J. Alloys Compd.*, 311 (2000) L5.
2. Y.B. Wang, W.K. Tang, F. Wang, C.P. Ding, S.M. Xu and R.H. Yu, *Int. J. Hydrogen Energy*, 43 (2018) 3244.
3. M. Dymek, M. Nowak, M. Jurczyk and H. Bala, *J. Alloys Compd.*, 749 (2018) 534.

4. Y. Li, X.W. Hou, C.X. Wang, L.N. Cheng, X.L. Feng and S.M. Han, *Int. J. Hydrogen Energy*, 43 (2018) 5104.
5. K.T. Moller, T.R. Jensen, E. Akiba and H.-W. Li, *Prog. Nat. Sci.–Mater.*, 27 (2017) 34.
6. Z.J. Gao, Y.C. Luo, R.F. Li, Z. Lin and L. Kang, *J. Power Sources*, 241 (2013) 509.
7. R.F. Li, J. Wan, F. Wang, C.P. Ding and R.H. Yu, *J. Power Sources*, 301 (2016) 229.
8. Z.J. Gao, B. Zhang, Y.C. Luo and H.-W. Li, *J. Taiwan Inst.Chem. Eng.*, 89 (2018) 183.
9. Z.J. Gao, Z.N. Yang, Y.T. Li, A.Q. Deng, Y.C. Luo and H.-W. Li, *Dalton Trans.*, 47 (2018) 16453.
10. Z.J. Gao, L. Kang and Y.C. Luo, *New J. Chem.*, 37 (2013) 1105.
11. Y.T. Li, F. Fang, X.B. Yu, Q.A. Zhang, L.Z. Ouyang, M. Zhu and D.L. Sun, *Acta Mater.*, 59 (2011) 1829.
12. Z.J. Gao, Y.C. Luo, Z. Lin, R.F. Li, J.Y. Wang and L. Kang, *J. Solid State Electrochem.*, 17 (2013) 727.
13. K. Iwase, N. Terashita, K. Mori and T. Ishigaki, *Inorg. Chem.*, 51 (2012) 11805.
14. K. Iwase, N. Terashita, K. Mori, S. Tashiro, H. Yokota and T. Suzuki, *Int. J. Hydrogen Energy*, 39 (2014) 12773.
15. K. Iwase, N. Terashita, K. Mori, S. Tsunokake and T. Ishigaki, *Int. J. Hydrogen Energy*, 37 (2012) 18095.
16. L. Zhang, W.K. Du, S.M. Han, Y. Li, S.Q. Yang, Y.M. Zhao, C. Wu and H.Z. Mu, *Electrochim. Acta.*, 173 (2015) 200.
17. X.L. Ding, Y.T. Li, F. Fang, D.L. Sun and Q.A. Zhang, *J. Mater. Chem. A*, 5 (2017) 5067.
18. W. Xiong, H.Z. Yan, L. Wang, X. Zhao, J. Li, B.Q. Li and Y. Wang, *Int. J. Hydrogen Energy*, 42 (2017) 15319.
19. H.Z. Yan, W. Xiong, L. Wang, B.Q. Li, J. Li and X. Zhao, *Int. J. Hydrogen Energy*, 42 (2017) 2257.
20. C.J. Xue, L. Zhang, Y.P. Fan, G.X. Fan, B.Z. Liu and S.M. Han, *Int. J. Hydrogen Energy*, 42 (2017) 6051.
21. J. Cao, Y.M. Zhao, L. Zhang, Z.R. Jia, W.F. Wang, Z.T. Dong, S.M. Han and Y. Li, *Int. J. Hydrogen Energy*, 43 (2018) 17800.
22. H.W. Zhang, X.Y. Zheng, X. Tian, Y. Liu and X.G. Li, *Prog. Nat. Sci.–Mater.*, 27 (2017) 50.
23. M.N. Guzik, B.C. Hauback and K. Yvon, *J. Solid State Chem.*, 186 (2012) 9.
24. R.A. Young, The Rietveld Method, Introduction to the Rietveld Method; R.A. Young Eds.; Oxford University Press Inc; New York, 1995, p.1.
25. J. Rodriguez-Carvajal, Abstract of the Satellite Meeting on Powder Diffraction, Congress of IUCr, Toulouse, France, 1990, p. l27.
26. J.J. Liu, S.M. Han, D. Han, Y. Li, S.Q. Yang, L. Zhang and Y.M. Zhao, *J. Power Sources*, 287 (2015) 237.
27. N. Cui and J.L. Luo, *Electrochim. Acta*, 45 (2000) 3973.
28. J. Balej, *Int. J. Hydrogen Energy*, 10 (1985) 365.
29. T. Ozaki, M. Kanemoto, T. Kakeya, Y. Kitano, M. Kuzuhara, M. Watada, S. Tanase and T. Sakai, *J. Alloys Compd.*, 446-447 (2007) 620.
30. Y.H. Zhang, Z.H. Hou, B.W. Li, H.P. Ren, G.F. Zhang and D.L. Zhao, *J. Alloys Compd.*, 537 (2012) 175.
31. F. Li, K. Young, T. Ouchi and M.A. Fetcenko, *J. Alloys Compd.*, 471 (2009) 371.